From high temperature phase formation to transition metal substitution in the Fe/Al Co (001) system

Dominique Dubaux, Florian Brix, Émilie Gaudry, Peter Gille, Marie-Cécile de Weerd, Vincent Fournée, Muriel Sicot, Julian Ledieu

From high temperature phase formation to transition metal substitution in the Fe/Al_9Co_2(001) system

D. Dubaux[a], F. Brix[a], É. Gaudry[a], P. Gille[b], M.-C de Weerd[a], V. Fournée[a], M. Sicot[a], J. Ledieu[a,*]

[a] *Université de Lorraine, CNRS, IJL, F-54000 Nancy, France*
[b] *Department of Earth and Environmental Sciences, Crystallography Section, Ludwig Maximilians Universität München, Theresienstr. 41, D-80333 München, Germany*

Abstract

We report the formation of several complex intermetallics as surface alloys upon the adsorption of Fe on Al_9Co_2(001) for different dosing conditions. Up to 4 monolayers equivalent (MLE) of Fe deposited on the substrate held at 593 K, the low energy electron diffraction pattern consists of a $(\sqrt{2} \times \sqrt{2})$R45° phase with two additional domain types rotated by ±8° from it. The scanning tunneling microscopy (STM) measurements show that these three types of domains have the same crystallographic structure. The lattice parameters and structural motifs point towards the formation of the high-temperature Al_8Fe_5 phase (γ-brass of Zn_8Cu_5-type structure). For Fe deposition between 593 K and 873 K, we have identified the formation of two phases, tentatively assigned to a ternary disordered $Al_9(Co,Fe)_2$ overlayer and to the monoclinic $Al_{13}Fe_4$(100). The stoichiometric evolution of the grown structures have been characterised by angle-resolved x-ray photoelectron spectroscopy measurements. Density functional theory based calculations have been performed to model the Al_8Fe_5(100)/Al_9Co_2(001) interface, its structural stability and to simulate the corresponding STM images.

Keywords: intermetallic thin film, high temperature phase, surface energy, complex interfaces, STM, DFT

1. Introduction

Complex metallic alloys (CMA), intermetallic compounds made of at least two elements, are fascinating materials which exhibit unique physical and chemical properties [1]. Built from highly symmetric clusters [2, 3], extensive works have been undertaken to address fundamental questions related for instance to their lattice dynamics [4], to their electronic structures [5, 6, 7] or to the mechanisms responsible for aperiodic long-range ordering [8]. With a wealth of CMA remaining to be discovered and the continuous exploration of phases [9], it is foreseen that new bulk and surface phenomena will emerge.

*Corresponding author
Email address: Julian.ledieu@univ-lorraine.fr (J. Ledieu)

For the determination of the electronic and crystallographic structures of Al-based CMA surfaces, millimeter-sized single crystals have commonly been used when available. These works have highlighted complex energy landscapes, characteristics exploited to propagate complexity in elemental and molecular thin films [10, 11, 12]. For specific systems and under particular growth conditions, CMA have also been formed voluntarily or fortuitously as surface alloys [13]. We can refer for instance to the formation of Al_4Cu_9 while aiming to form single element thin films on quasicrystalline and approximant surfaces [14, 15, 16]. When exploring the Al-Cu surface phase diagram, the growth of the same binary γ-brass phase was achieved for Al/Cu(111) with the epitaxial relationship determined [17]. Motivated by the promising properties of complex Al-Ir intermetallic phases as protective coating [18], the adsorption of Ir on Al(100) has been investigated under various deposition conditions and resulted in the formation of the Al_9Ir_2(001) oriented compound as surface alloys. Cross-sectional transmission electronic microscopy (TEM) measurements revealed a coherent growth of this CMA on Al(100) and shed lights on the mechanism leading to the observed epitaxial relationship among the two antagonists [19]. Furthermore, the growth of Al-rich CMA phases ($Al_{13}Fe_4$ and Al_5Fe_2) have been highlighted at the coating-substrate interface in hot dip aluminized steel parts, process used to limit corrosion and oxidation of cast-iron and steels [20]. As a model system, Fe adsorption on Al(100) has been carried out to investigate the possibility in growing CMA/Al interfaces and to determine which intermetallic will form. Unexpectedly, the Fe deposition on Al(100) resulted in the growth of a metastable Al_9Fe_2 phase [21]. Prior to this surface study, this binary phase was reported only once in cast material of an Al-Fe-Si alloy [22]. Both Al_9Ir_2(001) and Al_9Fe_2(001) oriented thin films adopt identical epitaxial relationships with the Al(100) substrate. These two intermetallics are considered as isostructural to the monoclinic Al_9Co_2 compound [23]. Their bulk structures are described along the c-axis by alternating pure Al layer and puckered Al+Transition metal (TM) layers. As most CMA, the bulk and surface electronic structures of Al_9Co_2 exhibit a pseudogap at the Fermi level resulting from a strong Brillouin zone-Fermi surface interaction combined with *sp-d* hybridization [24]. The topmost layer of the Al_9Co_2(001) surface is bulk-terminated at pure Al planes [24]. Although exhibiting a higher rumpling than Al(100) surface, these planes have been approximated as "Al(100)-like" layers due to shared similarities of the local atomic arrangements. The Fe adsorption on Al(100) results in the formation of Al_9Fe_2 phase, hence would a similar phase be obtained for Fe deposition on "Al(100)-like" layers at the Al_9Co_2(001) surface or would the growth of a $Al_9(Fe,Co)_2$(001) phase be favored instead of a sharp Al_9Co_2(001)/Al_9Fe_2(001) interface? In the first scenario, the results could be transferred to obtain a duplex coating of continuous structure but with a sharp chemical transition. In the other case, a random Fe distribution at Co sites could be expected in the near Al_9Co_2(001) surface region in accordance with the substitution reported in previous studies [25, 26]. Other alternatives are also foreseen including the growth of Al-rich CMAs like the $Al_{13}Fe_4$ and Al_5Fe_2 compounds without forgetting the high temperature phase Al_8Fe_5 [27, 28].

To test these hypotheses, we have carried out the adsorption of Fe on a clean Al_9Co_2(001) surface under ultra high vacuum conditions which remains up-to-now unexplored. With Fe and Co in competition, this study should highlight the stability of certain surface phases as a function of the deposition condi-

tions. The objectives are many-fold aiming to determine the resulting binary or ternary phases, the surface structures and the associated growth mode and mechanism. This approach could also lead to the formation of complex metallic alloys otherwise unavailable as single crystal by conventional growth techniques. To increase our understanding at the atomic level, this study will combine experimental methods including low energy electron diffraction (LEED), scanning tunnelling microscopy (STM), X-ray photoelectron spectroscopy (XPS) techniques with density functional theory (DFT) calculations.

In Section 2, we will describe the experimental and computational details. Following the adsorption of Fe on the $Al_9Co_2(001)$ intermetallic, the experimental and theoretical results will be presented in Section 3. The most significant results are discussed in Section 4 before the conclusion.

2. Experimental and Computational details

2.1. Experimental details

The Al_9Co_2 single crystal has been grown from an off-stoichiometric melt of composition $Al_{91}Co_9$. The Czochralski technique was applied using a seed crystal oriented such that the (001) plane is perpendicular to the pulling direction (for more details see [24]). After the growth, the crystal was oriented using back-scattered Laue X-ray diffraction and cut to obtain a $Al_9Co_2(001)$ oriented sample. The $Al_9Co_2(001)$ surface was polished with decreasing diamond grain sizes down to 1/4 µm followed by a final polishing step with a silica suspension (0.25 µm).

Once under ultra-high vacuum conditions (base pressure of 3.10^{-11} mbar), the preparation and characterization of the $Al_9Co_2(001)$ surface are performed in a multi-chamber setup equipped with a variable temperature scanning tunneling microscope (VT-STM) operated at room temperature, LEED and XPS techniques, allowing for a complete description of the near-surface compositions and structures. The STM images were recorded in constant tunneling current (I_t) mode while checking the influence of the bias voltage (V_b) polarity on the images. The XPS spectra have been measured using an hemispherical analyzer and a non-monochromatized Mg K_α X-ray source (1253.6 eV). Prior to each Fe deposition, the sample preparation consists of repeated cycles of Ar^+ ion sputtering at 2 keV for 30 min followed by annealing to 953 K for 90 min. The surface temperature was monitored through an optical pyrometer with an emissivity set to 0.35. The surface ordering and cleanliness are systematically verified using LEED and XPS techniques.

Fe atoms have been deposited from a high purity rod ($99.99 + wt\%$) inserted in an electron-beam evaporator. The pressure was kept below 5.10^{-10} mbar during the deposition. The temperature of the intermetallic sample was set between 593 and 873 K. The deposition rate, kept constant at $2.2.10^{-2}$ MLE/s for all experiments, has been calibrated by dosing Fe on Ag(111) and by measuring the fractional area covered by STM for successive Fe depositions. The adsorption of Fe on the $Al_9Co_2(001)$ surface is quoted as monolayer equivalent (MLE) where 1 MLE corresponds to the completion of a Fe monolayer on Ag(111) as monitored by STM. The near-surface composition has been monitored using angle-resolved XPS (AR-XPS) carried from 0 to 70 ° take-off angle with respect to surface normal.

2.2. Computational details

The structural optimizations and electronic structure calculations were performed within the DFT framework using the plane-wave pseudopotential method as implemented in the Vienna *Ab initio* Simulation Package (VASP)[29, 30, 31, 32]. We have applied the projector-augmented wave method (PAW) [33, 34] to describe the interaction between the valence electrons and the ionic core. Electronic exchange and correlation are described by the spin-polarized generalized gradient approximation (GGA-PBE) [35, 36]. Eight valence electrons were explicitly treated for Fe ($4s^1 3d^7$) and three for Al ($3s^2 3p^1$). To achieve a good precision of the calculations, total energies were minimized until the energies differences became less than 10^{-5} eV between two electronic cycles during the structural optimizations. Atomic structures - plotted using the VESTA software [37]- were relaxed using conjugate gradient algorithm until the Hellmann-Feynman forces were as low as 0.01 eV/Å. Bulk and slab calculations were performed using a 450 eV cut-off energy of the wave functions (E_{cut}) and Γ-centered k-point meshes 9×9×1 generated according to the Monkhorst-Pack scheme [38]. Symmetric slabs were built using the Atomic Simulation Environment (ASE) [39] using a slab thickness larger than 8.8 Å. Using the method described in our previous studies [40, 41], surface energies (γ) were calculated as a function of the Al chemical potential as follows:

$$2\gamma A = E^{slab} - N_{Fe^{slab}}\mu_{Fe} - N_{Al^{slab}}\mu_{Al} \quad (1)$$

where E^{slab} is the total energy of the slab, $N_{i^{slab}}$ are the number of i atoms in the slab and μ_i the chemical potentials of the elemental metals.

Interfaces between the $Al_9Co_2(001)$ surface and the Al_8Fe_5 thin film were built by depositing the adlayers as close as possible to the substrate. The Al_8Fe_5 unit cell is rotated by 45° with respect to the substrate unit cell. The lateral translation between the two antagonists is random for the various models considered, with a maximal proximity condition of 1.8 Å between neighboring atoms.

3. Results

3.1. The $Al_9Co_2(001)$ surface

Prior to Fe deposition, the $Al_9Co_2(001)$ surface has been prepared and characterised using STM, XPS and LEED techniques. The results obtained are consistent with the monoclinic structure defined in the $P2_1/c$ space group (Pearson symbol $mP22$). The Al_9Co_2 lattice parameters are a = 6.22 Å, b = 6.29 Å, c = 8.56 Å and β = 94.77° [23]. Similarly to previous reports [24, 42], the clean $Al_9Co_2(001)$ surface exhibits a sharp (1×1) LEED pattern with a low background. As measured from the calculated Fast Fourier transform (FFT) using high resolution STM images (not shown here), it corresponds in real space to a unit cell with a rectangular unit mesh dimension equal to a = 6.2 ±0.2 Å and b = 6.3 ±0.2 Å. The surface presents atomically flat terraces separated by a unique step height equal to 4.3 ±0.2 Å (not shown here), in agreement with half of the $d_{(001)}$ interplanar spacing of Al_9Co_2 [24]. As determined by experimental and *ab initio* methods [24], the (001) surface of the monoclinic intermetallic corresponds to a bulk truncation at pure and dense Al terminations. Despite the absence of TM atoms within the topmost surface layer, there exists a small

bias dependence of the STM contrast due to the local density of states affected by the covalent character of the Al-Co bonds (*sp-d* hybridization).

3.2. Fe adsorption on the Al_9Co_2(001) surface

3.2.1. Surface evolution upon dosing at 593 K

In this section, we report Fe adsorption experiments on the clean Al_9Co_2(001) surface held at T_{sub} = 593 K. Between 1 to 4 MLE Fe deposition, the LEED pattern displays the diffraction spots of the intermetallic substrate and additional ones associated with three types of rotational domains. As presented in Fig. 1(a), one domain type corresponds to an apparent $(\sqrt{2} \times \sqrt{2})$R45° phase represented by green reciprocal lattice vectors. Two other types of domains (domains 2 and 3 with respectively blue and red vectors) with sharp diffraction spots are rotated symmetrically by 8.0±0.5° from the [100] substrate direction. Thus, the orientation of domain 3 seems to induce a coincidence in reciprocal space between its (3,-1), (1,3), (4,2) spots and (2,-1), (1,2), (3,1) substrate diffraction spots respectively. Similarly, domain 2 would have its (3,1), (1,-3), (4,-2) spots close to or coinciding with (2,1), (1,-2), (3,-1) substrate spots respectively. Within our detection limit, no domain spot could be detected in the close vicinity of the (2,-1), (1,2), (2,1) and (1,-2) substrate spots upon increasing the LEED energy (dynamical inspection).

The STM measurements performed on the 1 MLE Fe dosed surface confirm the formation of three types of rotational domains. Moreover, under these dosing conditions, the step and terrace morphology of the Al_9Co_2(001) surface remains visible and the surface unit cell is still well-resolved (see top part in Fig. 1(b)). Among certain terraces, sub-nanometer deep pores have developed upon Fe adsorption, features not observed on the clean intermetallic surface (Fig. S1(a)). For a given terrace, the depth of the pore ranges between 3.0 to 3.5 Å with respect to the Al_9Co_2(001) topmost layer. As shown in Fig. 1(b), the domains resemble islands with a height measured from the calculated histogram at 1.2 Å on each terrace at positive bias. Each domain type exhibits a square surface unit mesh with a lattice parameter derived from Fast Fourier transform calculations equal to 9.0 ±0.5 Å. Although 3 types of rotational domains have been formed at the intermetallic surface, domain 3 and 2 will not coexist on the same terraces. Instead, each of these domains will appear alternatively on every other terraces along with the $(\sqrt{2} \times \sqrt{2})$R45° domain (always present and denoted as domain $\sqrt{2}$ in Fig. 1(b)). This distribution is reflected in the LEED pattern with comparable diffraction spots intensity between domain 3 and 2 and stronger spots for the $(\sqrt{2} \times \sqrt{2})$R45° domain present on all terraces. After a careful examination of the STM images, the atomic structure seems similar across the domains and related by symmetry operations. This symmetry relationship is illustrated in Fig. 1(c) where the local structures have been described using S-like motifs. The local motifs of domain 3 and domain 2 are inverted with respect to each other. As evidenced by the S-like symbol, this also applies between $(\sqrt{2} \times \sqrt{2})$R45° domains located on terraces separated by a single step height.

The STM images are bias dependent with the S-like motifs being replaced by a square pattern (see Fig. S1(b)). Adjacent domains are separated by domain boundaries imaged as a brighter contrast in positive bias. Alike domain type sharing a common boundary can be shifted from one another, i.e. there are sometimes out of registry.

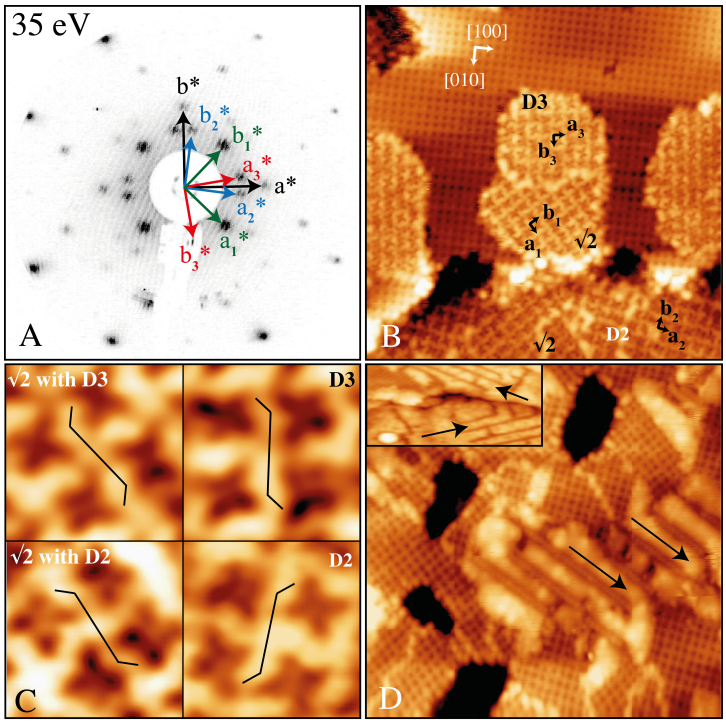

Figure 1: a) LEED pattern recording after 2 MLE Fe deposition on the $Al_9Co_2(001)$ held to 593 K. b) The three types of domains labelled $\sqrt{2}$, D2 and D3 are identified after 1 MLE Fe exposure using high resolution STM image (25 nm×25 nm). c) 2 nm×2 nm STM images of the local structures observed within each domain type with a S-like symbol superimposed on each motif (for (b-c) V_b= +1.0 V; I_t= 0.1 nA). d) 35 nm× 35 nm STM image obtained after 2 MLE Fe deposition (V_b= -1.2 V; I_t= 0.1 nA). Inset: STM image (30 nm× 14 nm) showing that the island orientation changes on consecutive terraces separated by a single step height.

From the lattice parameters measured experimentally and considering the Al-Fe phase diagram, the domains formed upon Fe deposition at 593 K could be attributed to the Al_8Fe_5 intermetallic phase, i.e. a γ-brass phase of Zn_8Cu_5 structure-type with a $I\bar{4}3m$ space group ($a = 8.9757$ Å). It is a high temperature phase in the Fe-Al system initially reported by Gwyer *et al.* [43] and structurally determined later by Vogel *et al.* [44].

Upon further Fe deposition, the density of domains is increasing as well as the pore density. This results in a fragmented surface with isolated group of joined domains (see Fig. S1(c)), hence leading to a surface with a pronounced 3-d character. On top of the largest isolated domains, the onset of another layer (brightest contrast) can be identified and corresponds to anisotropic shaped islands of about 2.0 Å in height with specific orientations (indicated by arrows) alternating between consecutive terraces (see Fig. 1(d) and Inset). No structural resolution could be obtained by STM within these islands, indicating either a small unit cell and/or a delocalized electronic density of states. The LEED is preserved up to 4 MLE with fainter spots attributed to the Al_8Fe_5 intermetallic phase. At 7 MLE, the LEED pattern has changed with only 8 diffraction spots visible at 50 eV, hence reflecting a less complex surface structure. Two square reciprocal lattices are needed to described the diffraction pattern orientated at

about ±26.5±0.5° from the Al_9Co_2[100] direction (see Fig. 2(a)). A comparison between LEED patterns recorded on the clean and Fe dosed surfaces under the exact same configuration reveals that the (1,0) and (0,1) broad spots of the new phase formed at 7 MLE Fe deposition are slightly off the (2,1) and (1,2) Al_9Co_2 substrate spots. The lattice constant measured from the LEED pattern is equal to 2.95 ±0.10 Å. The STM measurements reveal a 3-d surface consisting of stacking of islands (see Fig. 2(b)). The step heights that could be measured between two large islands are about 3.0 ±0.5 Å.

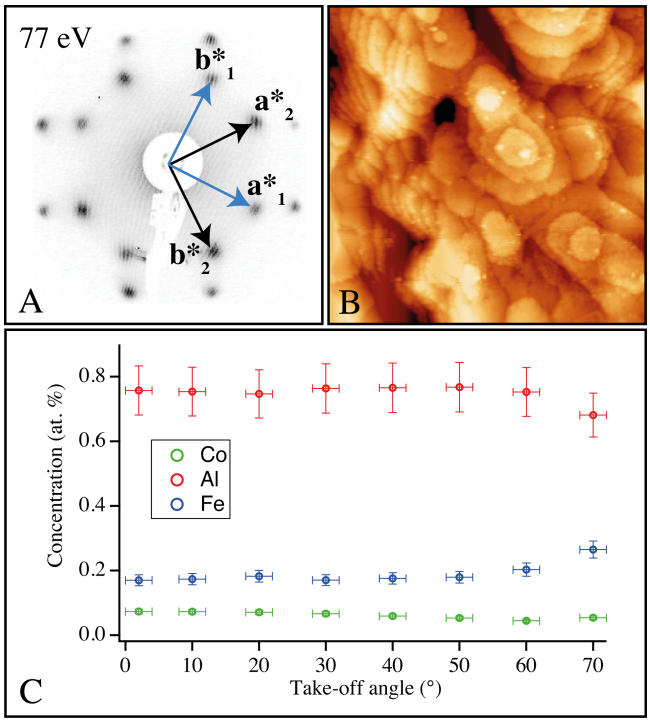

Figure 2: a) LEED pattern recording after 7 MLE Fe deposition on the Al_9Co_2(001) held to 593 K. b) The 7 MLE dosed surface investigated by STM (100 nm×100 nm) exhibits a pronounced 3-d character (V_b= -1.0 V; I_t= 0.1 nA). c) Variation of the elemental composition at the Al_9Co_2(001) surface as a function of the photoelectrons take-off angle for 2 MLE Fe deposition at 593 K.

Following the surface structural characterisation of the thin films, the surface chemical composition has been investigated as a function of MLE Fe deposition using AR-XPS with photoelectron take-off angles ranging from 0 to 70°. To this end, the removal of Mg K-α satellites and a Shirley background subtraction have been applied to the Al 2p, Fe 2$p_{3/2}$ and Co 2$p_{3/2}$ core level spectra. The measured area for each core level has been corrected by a normalization coefficient N which is calculated as follows:

$$N = \lambda \times \sigma \times ATF \tag{2}$$

where ATF corresponds to the analyser transmission function, σ is the photoionisation cross section and λ (Å) is the photoelectron inelastic mean free path. The latter is determined using the relationship that exists between the

kinetic energy (eV) and λ [45]:

$$\lambda = \frac{538d}{E_{kin}^2} + 0.13\sqrt{d^3 E_{kin}} \quad (3)$$

with d, the interlayer spacing of the material in Å and E_{kin} the kinetic energy of the photoelectron in eV.

Figure S2 presents the evolution of the peak area ratios among the Al $2p$, Co $2p_{3/2}$ and Fe $2p_{3/2}$ core levels as a function of Fe deposition. The substrate signals (Al $2p$ and Co $2p_{3/2}$) decrease continuously with increasing Fe exposure (see Fig. S2). However, the rate of decrease of the Al $2p$ signal is much lower than for the Co $2p_{3/2}$ signal. The Co $2p_{3/2}$ signal becomes very weak above 4 MLE (see Fig. S2) with the Al to Co ratio increasing with increasing Fe deposition. These results suggest the formation of Al-Fe phases upon successive Fe deposition at the near surface region when the sample is held to 593 K.

For 2 MLE, the AR-XPS measurements shown in Fig. 2(c) indicate a constant elemental composition while varying the sampling depth. Based on these results, surface segregation within the near surface region can be disregarded in this exposure regime. The stoichiometry derived from only Al and Fe core levels does not match the Al_8Fe_5 composition due to a remaining $Al_9Co_2(001)$ substrate contribution.

3.2.2. Modeling the $Al_8Fe_5(100)/Al_9Co_2(001)$ interface

To interpret further the atomic structures observed in the domains grown at 2 MLE (see Fig. 1), DFT calculations have been performed for several surface models derived from (in)complete Al_8Fe_5 bulk layers. The Al_8Fe_5 structure shown in Fig. 3 can be described as a stacking along the [100] direction of two distinct planes referred as G1 and G2. The other remaining planes are related to either G1 or G2 planes by symmetry operations. While G1 is characterised by square Al patterns, parallel rows of Fe can be distinguished within the denser G2 layers (see Fig. 3). Among the 6 models considered for the calculations of the relative surface energies (see Fig. S3), models 2 and 6 correspond to the complete G1 and G2 layers respectively. The other intermediate surface models are obtained by selectively removing atoms or group of atoms of comparable heights along the [100] direction.

As shown in Fig. 4, model 6 stands out from the other configurations with a much lower surface energy over the whole Al chemical potential range. If no chemical segregation or surface reconstruction occur, it is foreseen that the preparation of a Al_8Fe_5 oriented (100) single crystal would lead to a bulk truncation at G2 plane (see Fig. 4(b)), the latter being the most stable and the densest configuration among those considered. Following these surface energy calculations, simulated and experimental STM images of all models have been compared in order to associate the image contrasts to a surface structure. The STM image simulations have been performed within the Tersoff-Hamann approximation [46, 47], using the same bias voltage (V) as the experimental one ($V_b = \pm 1$V). The images were simulated using a constant current corresponding to that of the mean value calculated at 3 Å above the surface.

The simulated images for the 6 models (see Fig. 4(c) and Fig. S3) show little similarities with the experimental images. It is then expected that the adlayer thickness and its location above $Al_9Co_2(001)$ will have a great impact

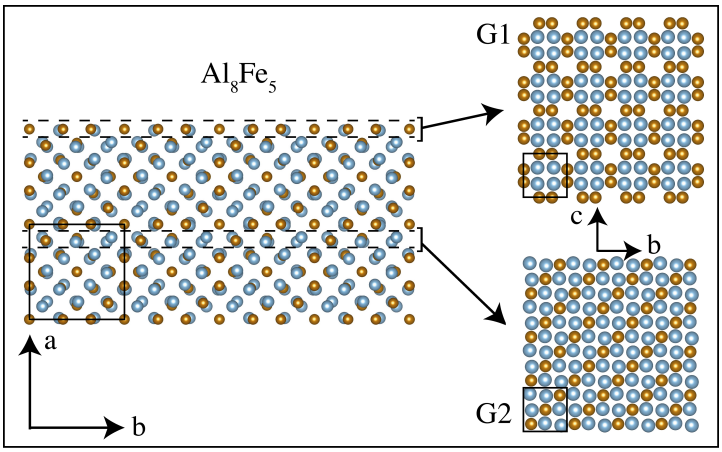

Figure 3: Left) Al_8Fe_5 bulk structure viewed along the [001] direction. Right) Two different types of (100) planes referred as G1 and G2 are present within the bulk model. The Al and Fe atoms are represented as light blue and brown spheres respectively.

on the resulting STM contrast. Moreover, the substrate rumpling and possible Fe diffusion beneath the topmost surface layers will probably lead to a system departing from an ideal truncated bulk model.

Considering these factors, several interfacial models have been generated and the corresponding simulated STM images have been calculated after structural relaxations (see Fig. S4 and S5). As expected, the models associated with a unique G1 or G2 layers deposited on an Al_9Co_2(001) F-type layer result in images drastically different to those obtained for the 6 models generated by bulk truncation (see Fig. S3). However, similarities among simulated images are recovered for thicker Al_8Fe_5 film. For instance, a close correspondence is found for the stacking sequence [48] G2G2G1G2 (Fig. S5) with model 6 (see Fig. 4(c)), hence confirming the strong impact of the film thickness on the STM image contrasts. Thus, the thickness of the Al_8Fe_5 film has been varied between 1 and 4 bulk planes within the modeled configurations. The second observation is related to the location of the Al_8Fe_5 layers with respect to Al_9Co_2(001) termination. As illustrated in Fig. 5, the lateral positioning of the Al_8Fe_5 G2 layer (idem for G1) considerably modifies the resulting simulated STM images which exhibit different local motifs. With such great variability originating from the many possible interfaces (translation, stacking sequences ...), only a limited amount of models could be tested.

Consequently, a precise interfacial model cannot be proposed. However, similarities between simulated and experimental images could be highlighted for several models including the model displayed in Fig. 5(a,d) for positive and negative bias. Here, the main contrast variations are attributed to the Fe positions appearing darker at negative bias.

Upon structural relaxation, the G2 adlayers remain more stable than G1 planes for which larger atomic displacements are present. This phenomenon can be related to the lower density of G1 plane. It translates into lower bonding strengths among G1 adlayer atoms, the influence of the substrate being then stronger. Compared to G1 plane, G2 adlayers have a higher Al content, element having the lowest surface energy. Interfaces with G1 plane cannot be disregarded

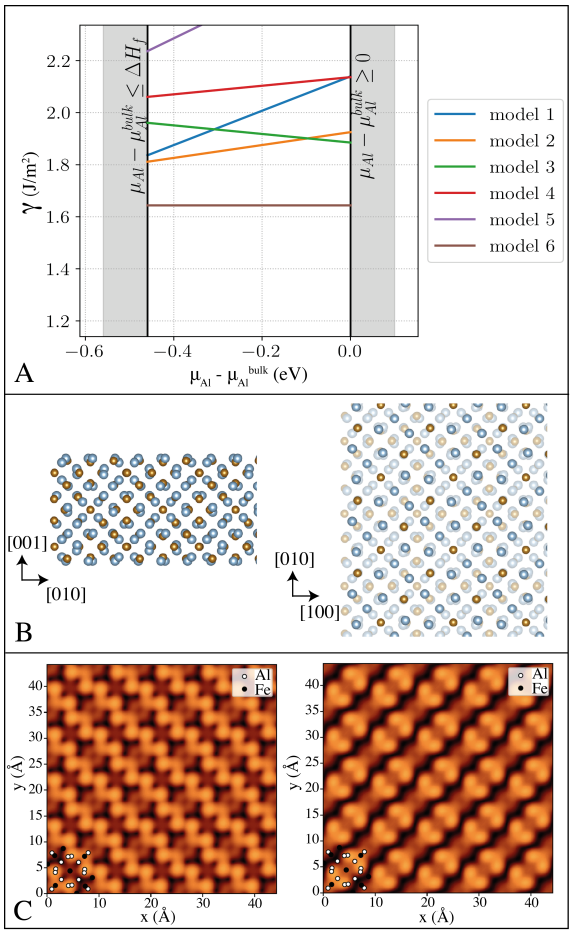

Figure 4: a) Surface energies calculated for the 6 models derived from the Al_8Fe_5 bulk structure as a function of the chemical potential of Al. b) Side (left) and top (right) views of model 6 where the Al and Fe atoms are represented as light blue and brown spheres respectively. c) Simulated STM images calculated for model 6 at +1 V (left) and -1 V (right).

at this stage due to the remaining configurational space to be explored. However, surface energy calculations point towards $Al_8Fe_5(100)$ terminated by G2 bulk plane. Finally, depending on the growth mechanism, alternative interfaces with Al_8Fe_5/ $Al_9Co_2(001)$ P-type layer should be considered in greater depth, which is beyond the scope of this study.

These *ab initio* calculations point clearly towards a relatively thin Al_8Fe_5 film where interfacial structural relaxation and adlayer lateral positioning impact greatly the resulting STM contrasts.

3.2.3. Adsorption within the high temperature regime

For T_{sub}= 873 K, the adsorption of 2 MLE Fe leads to the formation of additional surface structures and phases as evidenced by the LEED patterns. The diffraction pattern presented in Fig. 6(a) can be described by five reciprocal lattices. First, two rectangular unit meshes are rotated from each other by 90°. As they are mirror symmetric with respect to the a (and b) axis, this results in 4

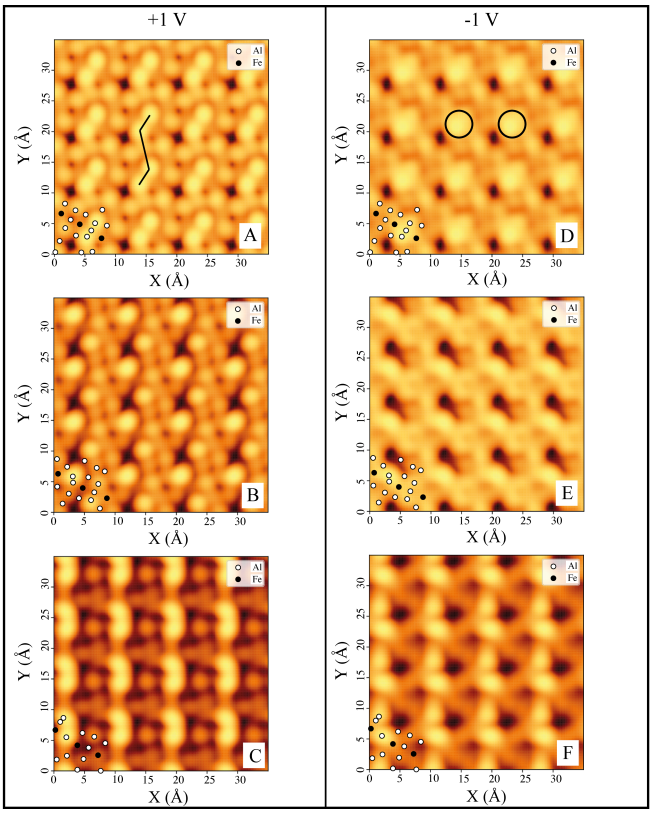

Figure 5: a) Simulated STM images obtained for three similar G2/Al_9Co_2(001) models at a-c) +1 V and d-f) -1V bias. Here, only the lateral position of G2 is changing among the models. The S-like symbol observed experimentally (see Fig. 1(c)) is also present on the simulated images as displayed in a).

types of domains. The angles between these 4 types of domains and the substrate a axis are equal to $\pm 18.5 \pm 1.0°$ for lattices labelled 1 and 3 and $\pm 71.5 \pm 1.0°$ for lattices labelled 2 and 4 (see Fig. 6(a)). For each domain type, the lattice parameters measured from the faint and broad diffraction spots are equal to a = 8.1±0.2 Å and b = 12.2±0.3 Å. The remaining sharp diffraction spots, well resolved on a larger energy scale, are supposedly related to the Al_9Co_2(001) surface. However, a close comparison with the diffraction pattern from the clean Al_9Co_2(001) surface clearly indicates a small lattice expansion of the a and b unit cell parameters by about +0.1 Å after high temperature Fe exposure (see Fig. 6(b)). We note that the plot profiles have been shifted and aligned on the (1,0) spot to better outline the lattice expansion. The asymmetry in the spot intensities originates from a sample misalignment that cannot be adjusted in that direction. Hence, it is likely that this small departure from the clean surface unit cell parameters originates from Fe insertion into the Al_9Co_2(001) surface.

In agreement with the LEED analysis, the STM results reveal the growth of a new phase with unit cell parameters measured from the calculated FFT equal to a = 8.0±0.3 Å and b = 12.4±0.5 Å. Within the Al-Fe system, these lattice parameters would fit with the rectangular unit cell of an $Al_{13}Fe_4$(100)

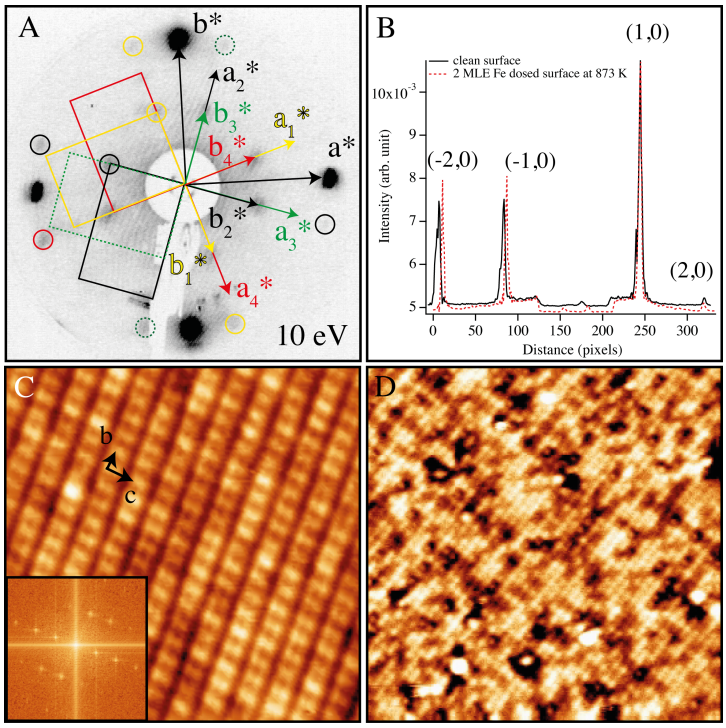

Figure 6: LEED pattern recorded after dosing 2 MLE Fe with the Al_9Co_2(001) surface held at 873 K. Several diffraction spots have been encircled in the domain colour they belong to. b) Plot profiles across the LEED spots for patterns recorded at 53 eV on the clean Al_9Co_2(001) and after 2 MLE Fe exposure with the sample at 873 K. c) 15 nm×15 nm high resolution STM image of the $Al_{13}Fe_4$(100) surface (V_b= -1.0 V; I_t= 0.11 nA). Inset: FFT calculated on a larger STM image (735 nm^2). d) 25 nm×25 nm High resolution STM image of the $Al_9(Co,Fe)_2$ phase (V_b= -1.4 V; I_t= 0.1 nA).

surface (b = 8.078 Å and c = 12.471 Å [49]). As seen in Fig. 6(c), the structure can be described by bright features decorating the vertices of a rectangular mesh. The STM images are bias dependent with the rectangular mesh being replaced by well-separated lines propagating along the $Al_{13}Fe_4$ [010] direction at positive bias (not shown here). Aside from the domains of this complex intermetallic phase, other regions correspond to the Fe exposed Al_9Co_2(001) surface at high temperature. The STM images of the unreconstructed surface present a heterogeneous contrast in Fig. 6(d), which is not observed on the clean Al_9Co_2(001) surface (see Fig.4 in [24]). The roughness (root mean square) across the images are below 0.15 Å at both positive and negative bias. These results indicate that Fe atoms are probably present within the surface planes, likely in substitution to some Co atoms. In other words, the surface structure observed by STM would be consistent with an $Al_9(Co,Fe)_2$ phase. Such random Fe substitution at Co sites would impact slightly the surface unit cell parameters, small effect observed on the LEED pattern (see Fig. 6(d)).

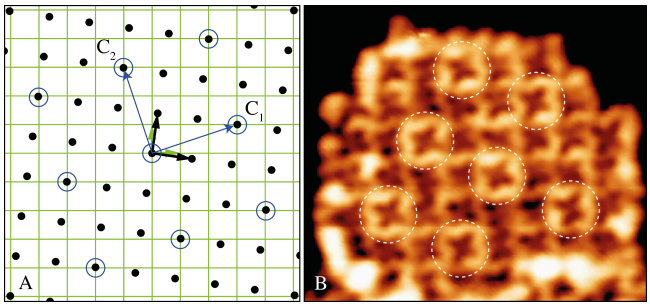

Figure 7: Schematic representation of the lattice site coincidence between the $Al_8Fe_5(100)$ (black spots) and the $Al_9Co_2(001)$ substrate (green lattice). The $Al_8Fe_5(100)$ is oriented as in D2. b) 8.1 nm×7.1 nm high resolution Fourier enhanced STM image presenting the Moiré pattern (dashed circles) observed in D3 (V_b= +1.0 V; I_t= 0.1 nA).

4. Discussion and Conclusion

We have investigated the adsorption of Fe on the $Al_9Co_2(001)$ complex metallic alloy surface. Depending on the Fe exposure and substrate temperature, several overlayer structures and phases have been identified and characterised using both experimental and numerical approaches. For room temperature deposition, the adatoms are trapped where they hit the surface, leading to a disordered thin film. At 593 K, the Fe diffusion is thermally activated and the growth of the high temperature Al_8Fe_5 phase occurs as isolated islands at low coverage. Stable as a surface alloy, this γ-brass phase exhibits three types of rotational domains. For the apparent $(\sqrt{2} \times \sqrt{2})$R45° domain to be really commensurate with the $Al_9Co_2(001)$ substrate, the alloy structure should have the following lattice parameters: $a = b = 8.84$ Å ($\sqrt{a^2_{Al_9Co_2} + b^2_{Al_9Co_2}}$) with α= 90.7°. Because the $Al_9Co_2(001)$ unit mesh is not square, this implies a compressive strain of 1.4% on the Al_8Fe_5 lattice constants with a slight distortion of the square lattice (0.7°). Concerning the other types of domains and within our detection limit in LEED, several diffraction spots appear in coincidence with $Al_9Co_2(001)$ spots. If no lattice distortion occurs, this translates in real space to coincidence at several lattice sites (see Fig. 7(a)). For instance, this can be achieved for a Al_8Fe_5 lattice contraction of 1.9% ($a = b = 8.80$ Å) and a rotation of -7.93° with respect to Al_9Co_2 [100] direction (a coincidence obtained at point C_1). Then, the [210] direction of domain 2 would be parallel to the [310] substrate direction. The lattice mismatch in the other direction would be below 1.0%. Alternatively, a coincidence at point C_2 in Fig. 7(a) while keeping a square structure would require a lattice constant of $a = b = 8.88$ Å with a lattice mismatch of 0.9% at point C_1. A comparable description applies to domain 3 with a rotation of +7.93° from the Al_9Co_2 [100] direction.

While the above scenarios are consistent with the STM and LEED analysis, other configurations including small lattice distortion with an average of the two above described lattices (8.84 Å) may occur and other techniques would be required to possibly determine this. Regardless of the configurations, the general trend points towards an Al_8Fe_5 overlayer slightly strained to accommodate for the stress imposed by the $Al_9Co_2(001)$ substrate. The interference of the different lattice spacing of domain 3 or 2 and the substrate along with a

specific rotation generates a Moiré pattern which can be distinguished in the STM images shown in Fig. 7(b). The Moiré manifested by brighter contrasts in the STM image is highlighted by dashed circles. With an edge length measured at 19.7±0.5 Å, this Moiré pattern originates from the lattice coincidence highlighted in Fig. 7(a). From the (3,1|-1,3) matrix relating the superstructure and the substrate, the Moiré unit cell is defined by $a_m = 19.68$ Å, $b_m = 19.86$ Å and $\alpha = 89.6°$, i.e. it can be denoted as a quasi $(\sqrt{10}\times\sqrt{10})$R18.6° structure. An identical Moiré with R-18.6° is present on the other domain type. While this coincidence at lattice sites would explained the domains orientations observed in the LEED pattern, it fails to explain the alternation of domain 3 and 2 across consecutive Al_9Co_2(001) terraces and the inverted S-shape within the unit cell in the domains.

To this end, we should first recall the surface structure of the Al_9Co_2(001) surface. Along the [001] direction, the structure can be described as a stacking of pure Al flat (F and F') and Al+Co puckered (P and P') layers in a *FPF'P'* sequence (see Fig. S6). As explained in Sec. 3.1, the Al_9Co_2(001) terminates at pure Al bulk planes which, while more rumpled, resemble "Al(100)-like" plane by their local motifs. Consequently, F and F' layers will appear alternatively on consecutive terraces. Due to the substrate space group ($P2_1/c$ space group), these two planes are related to each other by a 2_1 screw axis along b axis or by a glide operation along c axis. These symmetry operations result in two different orientations of the Al motifs across consecutive terraces at the Al_9Co_2(001) surface (see Fig. S6). When comparing the local motifs within $(\sqrt{2}\times\sqrt{2})$R45° domains across terraces, the overall shape is inverted or flipped. These observations are a direct consequence of the 2_1 screw axis present between F and F'. As domain 3 or domain 2 are respectively only present on one type of F-Layer, this motif flip is absent among alike oriented domain types. However, this effect reappears when comparing the motifs of domain 3 with those in domain 2.

To understand the non-coexistence of domain 3 and 2 on the same terrace, one Al_8Fe_5(100) bulk plane will be superimposed on a F-type layer. Along the [100] direction, two different bulk planes (G1 and G2) can be geometrically identified in the γ-brass phase (see Fig. 8). Here, we will consider only G1 plane but the same interpretation is valid with G2 layer. When superimposed on a F layer, G1 plane can be rotated by either + or -7.93° with respect to Al_9Co_2 [100] direction. In both cases and as deduced from the above analysis, a lattice site coincidence is present in the model for both orientations. However, the F plane decoration is such that at +7.93° (and not at -7.93°), additional close lattice site coincidences can be highlighted as demonstrated in Fig. 8(a-b). The combination of both Al_9Co_2(001) and Al_8Fe_5(100) layers results in local atomic configurations qualitatively similar within each overlayer unit cell. It is not strictly speaking periodic but highly similar if minute atomic relaxations both in and out-of-plane are permitted. A comparable atomic distribution is present for the $(\sqrt{2}\times\sqrt{2})$R45° domain and for domain 2 rotated by -7.93° superimposed on a F' layer. This arrangement similarities are reflected in the Al_8Fe_5 unit cell contrast which is identical by STM regardless of the domain orientations. How could such effect emerge at the length scale? Due to its resemblance with an "Al(100)" plane, the F plane structure can be approximated as consisting of Al square motifs. If these motifs define a "new" smaller surface unit mesh, then a near coincidence with the Al_8Fe_5(100) is obtained and related to a quasi (1,3|-

3,1) matrix. This close lattice match is responsible for the alternated domain type selection across terraces.

Above 4 MLE Fe deposition, a new cubic structure with $a = 2.95 \pm 0.10$ Å has been identified. Among the different possible phases formed, this lattice parameter would be consistent with the formation of a *B2* phase (CsCl-type structure). Due to the 3-d growth mode shown in Fig. 2(b), the XPS measurements remain affected by the $Al_9Co_2(001)$ surface as evidenced by the detection of about 1 at.% of Co (see Fig. S2). This limits the precise compositional determination of the grown thin film. A continuous solid-solution exists between AlFe and AlCo *B2* phases. However, considering the low Co content measured by XPS, the *B2* phase is likely to be close to AlFe under our dosing conditions, the Co atoms originating from the substrate. This phase would be the next one to appear in the Al-Fe phase diagram upon increasing the Fe content. Formed at 593 K, the (1×1) surface structure would be consistent with previous works reported on AlFe(100) single crystal [50]. It is also very likely that the surface would be terminated at Al pure layers [50]. This would explain the step height (equivalent to a full lattice parameter) measured between islands. Similar to the description for Al_8Fe_5 domain 3 and 2, only one of the two *B2* domains identified by LEED will be present for a given terrace. From a close inspection of STM images and from the domain orientations determined by LEED analysis, the *B2* unit cells are aligned with the Al square motifs present in F-type layers (see Fig. 8(c)). The Al layers present in the CsCl structure taken individually are also close to a Al(100) surface (lattice mismatch of 1.4%). This resemblance dictates the selection of the *B2* domain orientations. A comparable epitaxial growth was observed recently for the Fe/Al(100) system leading to the stabilisation of an Al_9Fe_2 surface phase based on a structural coincidence mechanism [21].

For the high temperature regime, the presence of two surface structures have been highlighted. The first one corresponds to the $Al_{13}Fe_4(100)$ approximant surface which consists of 4 types of domains. From the above analysis and as shown in Fig. 8(c), we believe that lattice site coincidence between the domains and the F-type layers will be responsible once more for the domains orientations with only 2 types of domains per terraces. As the sample temperature is increased, so is the Fe diffusion into the bulk of Al_9Co_2 sample. Hence for 2 MLE deposition at 873 K, the Fe content will be smaller than when the sample is held at 593 K (see AR-XPS in Fig. S7). *In fine*, the overall thin film composition will shift towards Al-rich phases, here stabilising the $Al_{13}Fe_4$ compound, i.e. the Al-richest stable phase in the Al-Fe system. This is consistent with the AR-XPS measurements which indicate lower content of Fe compared to Co, i.e. an inverse trend compared to the results presented in Fig. 2(c). The second structure coexisting in this temperature range is assigned to a $Al_9(Co,Fe)_2$ where the amount of Co substitution by Fe adsorbates is undetermined. However, a maximum solubility of 5% Fe in Al_9Co_2 has been reported at 1073 K while investigating the partial isothermal sections of the Al-rich corner of the Al-Co-Fe system [25]. As demonstrated previously [22], the existence of a metastable Al_9Fe_2 phase has been confirmed by electron microscopy and diffraction analysis. While a structural refinement is still lacking, the Al_9Fe_2 is considered as isostructural to the stable Al_9Co_2 phase. As measured on the LEED pattern, the $Al_9(Co,Fe)_2$ phase exhibits slightly larger unit mesh parameters. This is expected and consistent with the larger lattice parameters ($a = 6.32$ Å, $b = 6.35$ Å, $c = 8.69$ Å, and $\alpha =$

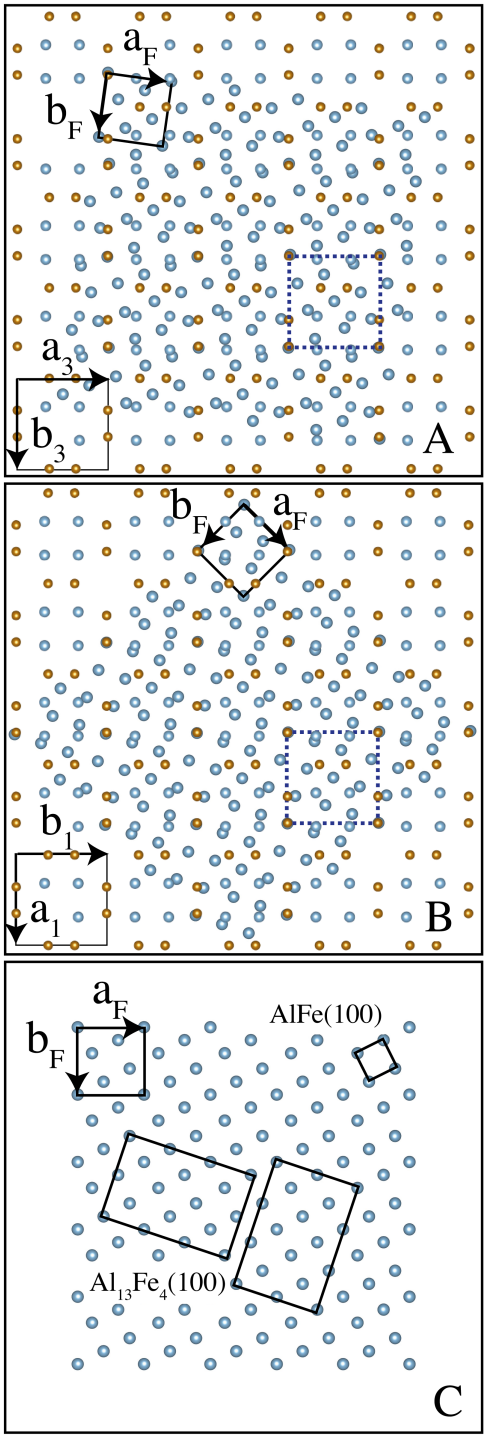

Figure 8: Sphere model representation of the $Al_8Fe_5(100)$ G1 plane superimposed on the F layer of the $Al_9Co_2(001)$ and rotated by +7.93° (a) and 45° (b). c) Representation of two $Al_{13}Fe_4(100)$ domains and of the AlFe *B2* unit cell on top of the F layer.

93.4°) of the Al_9Fe_2 compound. The random substitution at Co sites should result in small local lattice distortions reflected as a non uniform contrast variation across the STM images (see Fig. 6(d)). We foresee a similar scenario upon Co adsorption at high temperature (1073 K) on the $Al_{13}Fe_4(010)$ surface with the formation of an $Al_{13}(Fe,Co)_4(010)$ surface. Indeed, the monoclinic $Al_{13}Fe_4$ and $Al_{13}Co_4$ compounds form a continuous region of solid solution at 1073 K [25, 26]. Above 1073 K, the Al-Co-Fe phase diagram exhibits several three phase regions, one of them consisting of Al (liquid)+$Al_{13}(Fe,Co)_4$+Al_9Co_2 (with up to 5 at.%Fe) [26]. At 923 K, the monoclinic $Al_{13}Co_4$ is unstable and replaced by the orthorhombic $Al_{13}(Fe,Co)_4$ phase, a continuous solid solution being suppressed [51]. On the Al-rich corner of the ternary diagram, two three phase regions are then composed of o-$Al_{13}Co_4$+Al_9Co_2+m-$Al_{13}Fe_4$ and Al(liquid)+Al_9Co_2+m-$Al_{13}Fe_4$ under thermodynamic equilibrium. Once cooled down to room temperature, only two phases have been identified under our dosing conditions.

To conclude, the adsorption of Fe on the $Al_9Co_2(001)$ surface leads to the formation of a rich variety of phases. At moderate temperature and dosage, the epitaxial growth of $Al_8Fe_5(100)$ is achieved. The *ab initio* calculations demonstrate that the structure of the film cannot be considered as a purely truncated bulk Al_8Fe_5 as the adlayer undergoes a strong relaxation due to the interaction with the substrate. For some $Al_8Fe_5(100)/Al_9Co_2(001)$ configurations, the simulated images reproduce experimentally observed local motifs. While encouraging, further analysis including a genetic algorithm used in recent adsorption studies [52] would be a necessary step to identify the lowest energy configurations and discriminate among the various possible $Al_8Fe_5(100)/Al_9Co_2(001)$ interfacial models. In parallel, cross sectional investigations using TEM would be necessary to characterise the $Al_9(Co,Fe)_2(001)/Al_9Co_2(001)$ and $Al_{13}Fe_4(100)/Al_9Co_2(001)$ interfaces. Upon increasing Fe exposure, this high temperature compound of Zn_8Fe_5 type structure is replaced by a less complex *B2* AlFe phase (CsCl-type structure). At higher temperature and for 2 MLE, the $Al_{13}Fe_4(100)$ complex metallic alloy exhibits epitaxial relationships with the substrate and coexists with the $Al_9(Co,Fe)_2$ intermetallic. The topmost $Al_9Co_2(001)$ surface is composed of two types of pure Al bulk layer which appears alternately on terraces. These planes are related to each other by a glide operation along the c axis. These symmetry operations dictate the domain orientations of the phases formed and their alternated appearance on consecutive terraces. From the epitaxial relationships and the domain orientations derived from our analysis, it becomes possible to determine which of the two-types of Al bulk layer terminates the terrace, information not accessible up to now by STM measurements. The results presented here reveal also the surface structures of two CMA surfaces ($Al_8Fe_5(100)$, $Al_{13}Fe_4(100)$) which remain to be explored on single crystal surfaces.

Supporting Information Available

Supporting Information: STM and XPS measurements, surface models, model of the $Al_9Co_2(001)$ bulk structure, angle-resolved XPS and simulated STM images.

CRediT authorship contribution statement

D. Dubaux: Conceptualization, Methodology, Validation, Formal analysis, Investigation, Writing original draft, Visualisation. **F. Brix**: Methodology, Validation, Formal analysis, Investigation, Writing - Review & Editing. **É. Gaudry**: Methodology, Validation, Formal analysis, Investigation, Writing - Review & Editing, Funding acquisition. **P. Gille**: Resources, Writing-Review & Editing. **M.-C. de Weerd**: Resources, Writing-Review & Editing. **V. Fournée**: Validation, Writing-Review and Editing. **M. Sicot**: Methodology, Validation, Formal analysis, Writing-Review and Editing, Supervision. **J. Ledieu**: Conceptualization, Methodology, Validation, Formal analysis, Investigation, Writing-Review and Editing, Supervision, Funding acquisition.

Declaration of Competing Interests

The authors declare that they have no known competing financial interests or personal relationships that could have appeared to influence the work reported in this paper.

Acknowledgments

This work is supported by the European Integrated Center for the development of New Metallic Alloys and Compounds. Some of us acknowledge financial support through the COMETE project (COnception in silico de Matériaux pour l'EnvironnemenT et l'Energie) cofunded by the European Union under the program FEDER-FSE Lorraine et Massif des Vosges 2014-2020. High Performance Computing resources were provided by GENCI under the allocation 99642, as well as the EXPLOR center hosted by the Université de Lorraine (allocation 2017M4XXX0108).

References

[1] J.-M. Dubois, Properties - and applications of quasicrystals and complex metallic alloys, *Chem. Soc. Rev.* 41 (2012) 6760-6777.

[2] Ph. Scheid, C. Chatelier, J. Ledieu, V. Fournée, and É. Gaudry, Bonding network and stability of clusters: The case study of the $Al_{13}TM_4$ pseudo-10fold surfaces, *Acta Crystallogr. A* 75 (2019) 314-324.

[3] É. Gaudry, J. Ledieu, and V. Fournée, The role of three-dimensional bulk clusters in determining surface morphologies of intermetallic compounds: Quasicrystals to clathrates, *J. Chem. Phys.* 154 (2021) 124706 1-11.

[4] H. Euchner, T. Yamada, S. Rols, T. Ishimasa, Y. Kaneko, J. Ollivier, H. Schober, M. Mihalkovič, and M. de Boissieu, Tetrahedron dynamics in the icosahedral quasicrystals i-ZnMgSc and i-ZnAgSc and the cubic 1/1-approximant Zn_6Sc, *J. Phys.: Condens. Matter* 25 (2013) 115405 1-10.

[5] G. Trambly de Laissardière and T. Fujiwara, Electronic structure and transport in a model approximant of the decagonal quasicrystal Al-Cu-Co, *Phys. Rev. B* 50 (1994) 9843–9850.

[6] M. Krajčí, M. Windisch, J. Hafner, G. Kresse, and M. Mihalkovič, Atomic and electronic structure of icosahedral Al-Pd-Mn alloys and approximant phases, *Phys. Rev. B* 51 (1995) 17355–17378.

[7] G. Trambly de Laissardière, D. Nguyen-Manh, and D. Mayou, Electronic structure of complex Hume-Rothery phases and quasicrystals in transition metal aluminides, *Prog. Mater. Sci.* 50 (2005) 679–788.

[8] M. Mihalkovič and C. L. Henley, Empirical oscillating potentials for alloys from ab initio fits and the prediction of quasicrystal-related structures in the Al-Cu-Sc system, *Phys. Rev. B* 85 (2012) 092102 1-4.

[9] J. Dshemuchadse and W. Steurer, More statistics on intermetallic compounds – ternary phases, *Acta Crystallogr. A* 71 (2015) 335–345.

[10] J.A. Smerdon, The various modes of growth of metals on quasicrystals, *J. Phys.: Condens. Matter* 22 (2010) 433002 1-11.

[11] V. Fournée, J. Ledieu, M. Shimoda, M. Krajčí, H-R. Sharma, and R. McGrath, Thin film growth on quasicrystalline surfaces, *Isr. J. Chem.* 51 (2011) 1314–1325.

[12] J. Ledieu, É. Gaudry, and V. Fournée, Surfaces of Al-based complex metallic alloys: atomic structure, thin film growth and reactivity, *Sci. Technol. Adv. Mat.* 15 (2014) 034802 1-22.

[13] V. Fournée, J. Ledieu, É. Gaudry, H.R. Sharma, and R. McGrath, *Ultra-Thin Films on Complex Metallic Alloy Surfaces: A Perspective,* In: Kumar S., Aswal D. (eds) Recent Advances in Thin Films. Materials Horizons: From Nature to Nanomaterials. Springer, Singapore, 2020.

[14] M. Bielmann, A. Barranco, P. Ruffieux, O. Gröning, R. Fasel, R. Widmer, and P. Gröning, Formation of Al_4Cu_9 on the 5-fold surface of icosahedral AlPdMn, *Adv. Eng. Mat.* 7 (2005) 392–396.

[15] T. Duguet, J. Ledieu, J.M. Dubois, and V. Fournée, Surface alloys as interfacial layers between quasicrystalline and periodic materials, *J. Phys.: Condens. Matter* 20 (2008) 314009 1-8.

[16] R. Addou, A. K. Shukla, S. Alarcón Villaseca, É. Gaudry, Th. Deniozou, M. Heggen, M. Feuerbacher, R. Widmer, O. Gröning, V. Fournée, J.-M. Dubois, and J. Ledieu, Lead adsorption on the $Al_{13}Co_4$(100) surface: heterogeneous nucleation and pseudomorphic growth, *New J. Phys.* 13 (2011) 103011 1-19.

[17] T. Duguet, É. Gaudry, T. Deniozou, J. Ledieu, M.C. de Weerd, T. Belmonte, J.M. Dubois, and V. Fournée, Complex metallic surface alloys in the Al/Cu(111) system: an experimental and computational study, *Phys. Rev. B* 80 (2009) 205412 1-10.

[18] R. Darolia, *U.S. Patent 6,630,250,* B1 Oct. 7 (2003).

[19] J. Kadok, K. Pussi, S. Šturm, B. Ambrožič, É. Gaudry, M.-C. de Weerd, V. Fournée, and J. Ledieu, Epitaxial growth of Al_9Ir_2 intermetallic compound on Al(100): Mechanism and interface structure, *Phys. Rev. Mater.* 2 (2018) 043405 1-9.

[20] R. Mola, T. Bucki, and K. Wcisło, Characterization of Coatings on Grey Cast Iron Fabricated by Hot-dipping in Pure Al, $AlSi_{11}$ and $AlTi_5$ Alloys, *Arch. Foundry Eng.* 14 (2014) 85-90.

[21] D. Dubaux, É. Gaudry, M.-C. de Weerd, S. Šturm, M. Podlogar, J. Ghanbaja, S. Migot, V. Fournée, M. Sicot, and J. Ledieu, Metastable Al-Fe intermetallic stabilised by epitaxial relationship, *Appl. Surf. Sci.* 533 (2020) 147492 1-8.

[22] C. J. Simensen and R. Vellasamy, Determination of phases present in cast material of an Al-0.5 Wt.% Fe-0.2 Wt.% per cent Si alloy, *Z. Metallkde.* 68 (1977) 428–432.

[23] M. Boström, H. Rosner, Y. Prots, U. Burkhardt, and Y. Grin, The Co_2Al_9 structure type revisited, *Z. Anorg. Allg. Chem* 631 (2005) 534–541.

[24] S. Alarcón-Villaseca, J. Ledieu, L. Serkovic-Loli, M.-C. de Weerd, P. Gille, V. Fournée, J.-M. Dubois, and É. Gaudry, Structural investigation of the (001) surface of the Al_9Co_2 complex metallic alloy, *J. Phys. Chem. C* 115 (2011) 14922–14932.

[25] B. Grushko, W. Kowalski, and M. Surowiec, On the constitution of the AlCoFe alloy system, *J. Alloys Comp.* 491 (2010) L5–L7.

[26] L. Zhu, S. Soto-Medina, R. G. Hennig, and M. V. Manuel, Experimental investigation of the AlCoFe phase diagram over the whole composition range, *J. Alloys Comp.* 815 (2020) 152110 1-10.

[27] M. Turchanin, N. Kolchugina, A. Watson, and A. Kroupa, Al-Fe binary phase diagram evaluation · phase diagrams, crystallographic and thermodynamic data: Datasheet from msi eureka in springermaterials, Copyright 2013 MSI Materials Science International Services GmbH.

[28] X. Li, A. Scherf, M. Heilmaier, and F. Stein, The Al-rich part of the Fe-Al phase diagram, *J. Ph. Equilibria Diffus.* 37 (2016) 162–173.

[29] G. Kresse and J. Hafner, Ab initio molecular dynamics for liquid metals, *Phys. Rev. B* 47(1993) 558–561.

[30] G. Kresse and J. Hafner, Ab initio molecular-dynamics simulation of the liquid-metal-amorphous-semiconductor transition in germanium, *Phys. Rev. B* 49 (1994) 14251–14269.

[31] G. Kresse and J. Furthmüller, Efficient iterative schemes for *ab-initio* total-energy calculations using a plane-wave basis set, *Phys. Rev. B* 54 (1996) 11169–11186.

[32] G. Kresse and J. Furthmüller, Efficiency of *ab-initio* total-energy calculations for metals and semiconductors using a plane-wave basis set, *Comput. Mater. Sci.* 6 (1996) 15–50.

[33] P. Blöchl, Projector augmented-wave method, *Phys. Rev. B* 50 (1994) 17953–17979.

[34] G. Kresse and D. Joubert, From ultrasoft pseudopotentials to the projector augmented-wave method, *Phys. Rev. B* 59 (1999) 1758–1775.

[35] J.P. Perdew, K. Burke, and M. Ernzerhof, Generalized gradient approximation made simple, *Phys. Rev. Lett.* 77 (1996) 3865–3868.

[36] J.P. Perdew, K. Burke, and M. Ernzerhof, Generalized gradient approximation made simple, *Phys. Rev. Lett.* 78 (1997) 1396–1396.

[37] K. Momma and F. Izumi, VESTA 3 for three-dimensional visualization of crystal, volumetric and morphology data, *J. Appl. Cryst.* 44 (2000) 1272-1276.

[38] H.J. Monkhorst and J.D. Pack, Special points for Brillouin-zone integrations, *Phys. Rev. B* 78 (1976) 1396–1396.

[39] A. H. Larsen, J. J. Mortensen, J. Blomqvist, I. E. Castelli, R. Christensen, M. Dulak, J. Friis, M. N. Groves, B. Hammer, C. Hargus, E. D. Hermes, P. C. Jennings, P. B. Jensen, J. Kermode, J. R. Kitchin, E. L. Kolsbjerg, J. Kubal, K. Kaasbjerg, S. Lysgaard, J. B. Maronsson, T. Maxson, T. Olsen, L. Pastewka, A. Peterson, C. Rostgaard, J. Schiotz, O. Schütt, M. Strange, K. S. Thygesen, T. Vegge, L. Vilhelmsen, M. Walter, Z. Zeng, and K. W Jacobsen, The atomic simulation environment - a Python library for working with atoms, *J. Phys.: Condens. Matter* 29 (2017) 273002 1-59.

[40] F. Brix, R. Simon, and É. Gaudry, The (010) surface of the $Al_{45}Cr_7$ complex intermetallic compound: insights from density functional theory, *Z. Anorg. Allg. Chem.* 646 (2020) 1176–1182.

[41] L. Boulley, D. Kandaskalov, M.-C. de Weerd, S. Migot, J. Ghanbaja, S. Šturm, P. Boulet, J. Ledieu, É. Gaudry, and V. Fournée, Investigation of the (100) and (001) surfaces of the Al_5Fe_2 intermetallic compound, *Appl. Surf. Sci.* 542 (2021) 148540 1-11.

[42] J. Ledieu, É. Gaudry, M.-C. de Weerd, P. Gille, R. D. Diehl, and V. Fournée, C_{60} superstructure and carbide formation on the Al-terminated $Al_9Co_2(001)$ surface, *Phys. Rev. B* 91 (2015) 155418 1-13.

[43] A.G.C. Gwyer, Über die Legierungen des Aluminiums mit Kupfer, Eisen, Nickel, Kobalt, Blei und Cadmium, *Z. Anorg. Chem.* 57 (1908) 113-153.

[44] S.C. Vogel, F. Stein, and M. Palm, Investigation of the ε phase in the Fe–Al system by high-temperature neutron diffraction, *Appl. Phys. A* 99 (2010) 607-611.

[45] M. P. Seah and W. A. Dench, Quantitative electron spectroscopy of surfaces: A standard data base for electron inelastic mean free paths in solids, *Surf. Interface Anal.* 1 (1979) 2-11.

[46] J. Tersoff and D. R. Hamann, Theory and application for the scanning tunneling microscope, *Phys. Rev. Lett.* 50 (1983) 1998–2001.

[47] J. Tersoff and D. R. Hamann, Theory of the scanning tunneling microscope, *Phys. Rev. B* 31 (1985) 805–813.

[48] The stacking sequence considered in the calculations obeys the bulk plane sequence. Consequently, consecutive G2 layers will be related by symmetry operations following the structural bulk model.

[49] J. Grin, U. Burkhardt, M. Ellner, and K. Peters, Crystal structure of orthorhombic Co_4Al_{13}, *J. Alloys Comp.* 206 (1994) 243-247.

[50] L. Hammer, H. Graupner, V. Blum, K. Heinz, G.W. Ownby, and D.M. Zehner, Segregation phenomena on surfaces of the ordered bimetallic alloy FeAl, *Surf. Sci.* 412-413 (1998) 69–81.

[51] T. Kozakai, R. Okamoto, and T. Miyazaki, Phase equilibria in the Fe-Al-Co ternary system at 923 K, *Z. Metallkd.* 90 (1999) 261-266.

[52] F. Brix and É. Gaudry, Two-dimensional metal structures revealed by evolutionary computations: $Pb/Al_{13}Co_4(100)$ as a case study, *J. Vac. Sci. Technol. A* 40 (2022) 012203.